

LETTER TO THE EDITOR

The nature of the X-ray filaments around bow shock pulsar wind nebulae

Barbara Olmi^{1,2}, Elena Amato^{1,3}, Rino Bandiera¹ and Pasquale Blasi^{4,5}

¹ INAF - Osservatorio Astrofisico di Arcetri, Largo E. Fermi 5, I-50125 Firenze, Italy

² INAF - Osservatorio Astronomico di Palermo, Piazza del Parlamento 1, I-90134 Palermo, Italy

³ Università degli Studi di Firenze, Via Sansone 1, 50019, Sesto Fiorentino (FI), Italy

⁴ GSSI - Gran Sasso Science Institute, Viale F. Crispi 7 - I-67100 L' Aquila, Italy

⁵ INFN-Laboratori Nazionali del Gran Sasso, Via G. Acitelli 22, Assergi (AQ), Italy
e-mail: barbara.olmi@inaf.it, elena.amato@inaf.it, pasquale.blasi@gssi.it

March 7, 2024

ABSTRACT

Context. We propose that the X-ray filaments emerging from selected bow shock pulsar wind nebulae are due to a charge-separated outflow of electrons and/or positrons escaping the nebula and propagating along the local Galactic magnetic field.

Aims. The X-ray brightness, length, and thickness of filaments are all accounted for if a nonresonant streaming instability is excited.

Methods. This is possible if particles are released in the interstellar medium as a collimated beam, as would be expected in a reconnection region between the nebular and interstellar magnetic fields.

Results. We successfully test this idea on the Guitar Nebula filament and discuss other cases.

Conclusions. These filaments provide the best diagnostics available for particle escape from evolved pulsar wind nebulae, a process essential to assessing the contribution of these sources to cosmic ray positrons. The same phenomenology might govern the occurrence of TeV halos and their importance for cosmic ray transport.

Key words. Acceleration of particles, Instabilities, Magnetic fields, Radiation mechanisms: non-thermal, Relativistic processes, pulsars: general, cosmic rays, ISM: supernova remnants.

1. Introduction

An increasing number of bow shock pulsar wind nebulae (BSPWNe) shows evidence of filamentary X-ray structures (Hui & Becker 2007; Pavan et al. 2014; Temim et al. 2015; Klingler et al. 2016, 2018; Medvedev et al. 2019; Marelli et al. 2019; Bordas & Zhang 2020; Zhang et al. 2020; Klingler et al. 2020; de Vries & Romani 2022) protruding in the interstellar medium (ISM). The best characterized examples are the Guitar Nebula (Hui & Becker 2007; de Vries et al. 2022), PSR J2030+4415 (de Vries & Romani 2020; de Vries et al. 2022), and the Lighthouse Nebula (Pavan et al. 2014, 2016; Klingler et al. 2023). The filaments appear elongated in one direction for a distance ranging from 0.6 pc in the case of the Guitar Nebula to ~ 15 pc in the case of the Lighthouse, with relatively mild morphological fluctuations. The filaments' thickness is very small (from less than 1% of the length to $\sim 10\%$). The spectrum and morphology of the X-ray emission are compatible with synchrotron radiation of very high-energy leptons in a magnetic field that is substantially larger than the typical interstellar magnetic field (typically by a factor of ~ 10), a possible indication (Bandiera 2008) that some type of instability is excited by particles escaping the nebula (Olmi 2023), leading to magnetic field amplification. In turn, this can account for the thickness of the filaments as a consequence of severe synchrotron energy losses. This qualitatively appealing picture

needs a quantitative connection with known instabilities and with the actual energetics of the particles leaving the BSPWN.

Here we show that the length and thickness of the filaments require specific conditions that can only be satisfied if 1) electrons and positrons with sufficiently high energies are spatially charge-separated when leaving the BSPWN (Olmi & Bucciantini 2019, 2023), and 2) they are numerous enough to excite the nonresonant hybrid instability (Bell 2004) (NRI). Neither of these conditions is trivial: charge separation can only occur for pairs with energy sufficiently close to the maximum potential drop (MPD) of the pulsar, a condition that severely constrains the current density available to excite the instability.

We make the case that the electrons (or positrons) that escape the BSPWN may be focused in a narrow angle when leaving the source, and propagate along the local Galactic magnetic field (GMF) lines. The angular collimation is important in that it confines particles in a region with a small cross section, which in turn increases the current density. The excitation requires that the energy density associated with the particles dominating the current be larger than that of the preexisting magnetic field (Bell 2004) (in this case the GMF).

The nonresonant nature of the instability is a crucial ingredient in this context: the lack of scattering allows the

current-carrying particles to stream away from the BSPWN at speed close to that of light (c), thereby filling a filament for a length of order $\sim c\tau_{CR}$, where τ_{CR} is the time needed for the saturation of the instability. During this phase, the perturbed magnetic field keeps growing, possibly beyond the average Galactic value, on scales much smaller than the Larmor radius of the particles dominating the current. At saturation, or close to it, the nonlinear evolution of the instability drives power on large scales (Bell 2004), and eventually on scales comparable to the Larmor radius of the particles in the amplified field. At this point, particles start scattering efficiently and rapidly isotropize. The synchrotron emission of these electrons or positrons in the amplified field is expected to produce the X-rays that we observe from a region of length $\sim c\tau_{CR}$.

The proper motion of the pulsar is characterized by the pulsar velocity, V_{psr} , and the (typically large) angle, θ_f , that it forms with the local GMF (which is assumed to coincide in direction with the filament elongation). This would shape the emission region as a wide stripe, unless the emitting particles suffer synchrotron losses on a timescale, $\tau_{\text{cross}} = w_f/(V_{\text{psr}} \sin \theta_f)$, with w_f being the filament width.

Imposing $\tau_{\text{loss}} = \tau_{\text{cross}}$ returns the strength of the magnetic field in the filament, that must be compared with the value inferred from the saturation of the NRI. We show that the picture we are proposing is able to describe in a coherent way the length, thickness, and luminosity of the observed filaments.

2. Physical model of the filament

The discussion that follows aims at a quantitative description of three observables: (i) the length of the feature, L_f , (ii) its transverse thickness, $w_f \ll L_f$, and (iii) the observed X-ray luminosity in a given energy band, $L_{X_1-X_2}$. To date, the filaments have only been reliably measured in a handful of sources: the Guitar Nebula, the Lighthouse, and J2030+4415. These will be our benchmark cases. As was discussed early on (Bandiera 2008), the small filament widths require that the magnetic field inside these structures be larger than the GMF (typically by a factor of ~ 10) so that synchrotron losses are fast enough. At the same time, however, the radiating particles must reach distances from the pulsar much larger than the thickness of the filaments. This latter requirement suggests that the instability responsible for magnetic amplification is nonresonant. A resonant instability would in fact limit the particle motion to a few Larmor radii from the pulsar, due to effective resonant scattering, which is incompatible with the observed length. Here we show that the excitation of the current-driven NRI (Bell 2004) satisfies all these conditions and provides a suitable explanation of the observed phenomena.

While BSPWNe are expected to produce an equal number of electrons and positrons, it has been shown that particles with different charges escape the nebula along different paths (Olmi & Bucciantini 2019) at energies $\lesssim mc^2\gamma_{\text{MPD}}$, where the Lorentz factor corresponding to the MPD is

$$\gamma_{\text{MPD}} = \frac{e}{mc^2} \sqrt{\frac{\dot{E}}{c}}. \quad (1)$$

m and e are the electron mass and charge, respectively, and \dot{E} is the spin down luminosity of the pulsar. The current

associated with the escaping particles can be expressed as $j_p = e \epsilon \dot{E}/(m c^2 \gamma_{\text{esc}} A)$, where ϵ is the fraction of \dot{E} carried by the escaping particles, γ_{esc} is the minimum energy of the escaping particle, and $A = \pi R^2$ is the area at the base of the filament. The current can then be written as

$$j_p = \epsilon \frac{m c^3}{e \pi R^2} \frac{\gamma_{\text{MPD}}^2}{\gamma_{\text{esc}}}. \quad (2)$$

The NRI excites perturbations that in the linear and early nonlinear phases grow on small scales, with the maximum growth occurring at

$$k_{\text{max}} = \frac{4\pi}{B_0 c} j_p = \frac{4\epsilon}{R^2} \frac{c}{\Omega_c} \frac{\gamma_{\text{MPD}}^2}{\gamma_{\text{esc}}}, \quad (3)$$

at a rate,

$$\tau_{CR}^{-1} = k_{\text{max}} v_A = \frac{4\epsilon}{R^2} \frac{c^2}{\Omega_c} \frac{v_A}{c} \frac{\gamma_{\text{MPD}}^2}{\gamma_{\text{esc}}}, \quad (4)$$

where $v_A = B_0/\sqrt{4\pi\rho_{\text{ISM}}}$ is the Alfvén speed in the ISM with mass density ρ_{ISM} and $\Omega_c = eB_0/(mc)$ is the electron cyclotron frequency in the unperturbed ambient field, B_0 .

The condition for these modes to be excited is $k_{\text{max}} R_L > 1$, with $R_L = m c^2 \gamma_{\text{esc}}/(e B_0)$ the Larmor radius of the particles with γ_{esc} . The inequality can be rewritten as

$$\epsilon > \epsilon_{\text{lim}} = \frac{R^2 \Omega_c^2}{4c^2 \gamma_{\text{MPD}}^2} = \frac{1}{4} \frac{R^2}{R_{L, \text{MPD}}^2}, \quad (5)$$

where $R_{L, \text{MPD}} = m c^2 \gamma_{\text{MPD}}/(e B_0)$. Excitement of the NRI requires the energy density carried by the electric current to locally exceed that of the ambient magnetic field. This is reflected in a lower limit on the fraction of \dot{E} that needs to be channelled into the tube: once $\epsilon > \epsilon_{\text{lim}}$, the NRI is excited. The saturation of the NRI has been the subject of much literature: as was already found in the seminal work on this instability (Bell 2004), the growth of the unstable modes, associated with scales much smaller than R_L , is also accompanied by power deposition at larger scales, until there is power on scales comparable to the Larmor radius of the particles dominating the current calculated in the amplified field, ΔB . At that point, scattering becomes important and the current is disrupted. This condition reads as $k_{\text{max}}^* R_L^* = 1$, where $k_{\text{max}}^* = 4\pi j_p/(c\Delta B)$ and $R_L^* = m c^2 \gamma_{\text{esc}}/(e \Delta B)$, and it leads to

$$\left(\frac{\Delta B}{B_0}\right)^2 = \frac{\epsilon}{\epsilon_{\text{lim}}}. \quad (6)$$

It is important to keep in mind that during the exponential growth of the instability the perturbations remain on scales much smaller than the resonant scale, so that scattering is inhibited and, in the first approximation, the motion of the particles can be pictured as quasi-ballistic. We see a posteriori that a rather small collimation angle, α , of the injected particles is required and the longitudinal speed of the particles in the quasi-ballistic phase is $\sim c$. This phase lasts for a few e-folds of the instability, ~ 5 (Bell 2004), so that particles move along the magnetic field for a length,

$$\begin{aligned} L_f &\approx 5c\tau_{CR} = \frac{5c}{\Omega_c} \left(\frac{c}{v_A}\right) \left(\frac{\epsilon}{\epsilon_{\text{lim}}}\right)^{-1} \gamma_{\text{esc}} \\ &\simeq 422 \text{ pc} \left(\frac{\epsilon}{\epsilon_{\text{lim}}}\right)^{-1} \gamma_7 n_1^{1/2} B_3^{-2}, \end{aligned} \quad (7)$$

where in the last equality we have introduced $\gamma_7 = \gamma_{\text{esc}}/10^7$, $B_3 = B_0/3 \mu\text{G}$, and $n_1 = \rho_{\text{ISM}}/(1 m_p \text{cm}^{-3})$, with m_p the proton mass.

Within the assumed scenario, one can use Eq. 6 and Eq. 7 to relate the strength of the amplified magnetic field to the measured length of the filament. The result is

$$\Delta B \simeq 62 \mu\text{G} n_1^{1/4} \gamma_7^{1/2} \left(\frac{L_f}{\text{pc}} \right)^{-1/2}, \quad (8)$$

which, as expected for the NRI, is independent of the initial value of the field, B_0 .

A crucial ingredient in building a physical interpretation of the filaments is the motion of the pulsar with velocity V_{psr} . In the synchrotron loss time the pulsar has travelled a distance,

$$\begin{aligned} d_{\text{sync}}(\gamma) &= V_{\text{psr}} \sin \theta_f \tau_{\text{sync}}(\gamma) = \\ &= 5.7 \times 10^{-2} \text{ pc} \sin \theta_f n_1^{-3/8} \gamma_7^{-3/4} \\ &E_{\text{X,keV}}^{-1/2} \left(\frac{V_{\text{psr}}}{500 \text{ km s}^{-1}} \right) \left(\frac{L_f}{\text{pc}} \right)^{3/4}. \end{aligned} \quad (9)$$

In our scenario, $d_{\text{sync}}(\gamma_X)$ is interpreted as the measured thickness of the filament, w_f , and it allows one to derive γ_{esc} :

$$\begin{aligned} \gamma_{\text{esc}} &= 4.5 \times 10^5 \sin \theta_f^{4/3} n_1^{-1/2} E_{\text{X,keV}}^{-2/3} \\ &\left(\frac{V_{\text{psr}}}{500 \text{ km s}^{-1}} \right)^{4/3} \left(\frac{L_f}{\text{pc}} \right) \left(\frac{w_f}{\text{pc}} \right)^{-4/3}, \end{aligned} \quad (10)$$

which turns out to depend only on directly observed quantities, except for the density. Lacking better constraints, the latter can be derived by measuring the standoff distance, d_0 , defined by the balance between the pulsar wind energy flux and the ISM ram pressure: $\dot{E}/(4\pi c d_0^2) = \rho_{\text{ISM}} V_{\text{psr}}^2$. We can then express the Lorentz factor of the current-carrying particles as a function of observed quantities alone. This closes the system of equations.

Finally, we can make use of the observed X-ray luminosity to prove that the global picture presented above is meaningful. If the spectrum of the escaping particles reflects the power law behaviour that is typically observed in PWNe (Torres et al. 2014), one expects that if $\gamma_{\text{esc}} \geq \gamma_b \sim 5 \times 10^5$, then the number of injected particles per unit energy and time interval can be written as $Q(\gamma) = Q_0(\gamma/\gamma_b)^{-p}$, where $p \simeq 2.2 - 2.5$ is the high-energy particle injection index and Q_0 is a normalization constant that can be obtained by assuming that a fraction, η , of the power emitted by the pulsar goes into particles with $\gamma \geq \gamma_b$:

$$\begin{aligned} \eta \dot{E} &= m^2 c^4 \int_{\gamma_b}^{\gamma_{\text{MPD}}} Q_0 \left(\frac{\gamma}{\gamma_b} \right)^{-p} \gamma d\gamma \\ \rightarrow Q_0 &= \frac{p-2}{[1 - (\gamma_b/\gamma_{\text{MPD}})^{p-2}]} \frac{\eta \dot{E}}{(m c^2 \gamma_b)^2}. \end{aligned} \quad (11)$$

Similarly, the energy injected in the form of particles with $\gamma \geq \gamma_{\text{esc}}$, namely the particles that escape the nebula and end up in the feature, is

$$\begin{aligned} \epsilon \dot{E} &= \int_{\gamma_{\text{esc}}}^{\gamma_{\text{MPD}}} Q_0 \left(\frac{\gamma}{\gamma_b} \right)^{-p} \gamma d\gamma \\ \rightarrow \epsilon &= \eta \left(\frac{\gamma_b}{\gamma_{\text{esc}}} \right)^{p-2} \left(\frac{1 - (\gamma_{\text{esc}}/\gamma_{\text{MPD}})^{p-2}}{1 - (\gamma_b/\gamma_{\text{MPD}})^{p-2}} \right), \end{aligned} \quad (12)$$

where we used Eq. 11 for Q_0 . Under our assumptions, these particles will radiate all their energy in the feature, so that the X-ray luminosity in the energy range $E_{X_1} - E_{X_2}$ can be written as

$$\begin{aligned} L_{X_1-X_2} &= (m c^2)^2 \int_{\gamma_{X_1}}^{\gamma_{X_2}} Q(\gamma) \gamma d\gamma = \\ &= \epsilon \dot{E} \left[\frac{1 - (\gamma_{X_1}/\gamma_{X_2})^{p-2}}{1 - (\gamma_{\text{esc}}/\gamma_{\text{MPD}})^{p-2}} \right] \left(\frac{\gamma_{\text{esc}}}{\gamma_{X_1}} \right)^{p-2}, \end{aligned} \quad (13)$$

where $\gamma_{X_i} \geq \gamma_{\text{esc}}$ is the Lorentz factor of a lepton that, in the amplified magnetic field, ΔB , emits synchrotron radiation in the observed energy interval. The assumption underlying Eq.13 is that the life of the emitting particles is limited by synchrotron losses. From the previous equation we then express our last unknown parameter, ϵ , in terms of measured quantities alone:

$$\epsilon = \frac{L_{X_1-X_2}}{\dot{E}} \left[\frac{1 - (\gamma_{\text{esc}}/\gamma_{\text{MPD}})^{p-2}}{1 - (\gamma_{X_1}/\gamma_{X_2})^{p-2}} \right] \left(\frac{\gamma_{X_1}}{\gamma_{\text{esc}}} \right)^{p-2}. \quad (14)$$

This estimate assumes that the velocity distribution of particles is isotropic. As is shown in App. A, this is a reasonable approximation.

Once saturation of the NRI has been reached (after a time of $\sim 5\tau_{\text{CR}}$), the motion of the particles with Lorentz factor γ_{esc} is no longer ballistic, since scattering causes the particles to diffuse, with a diffusion coefficient that can be estimated as

$$\begin{aligned} D(\gamma_{\text{esc}}) &= \frac{1}{3} \frac{m c^3 \gamma_{\text{esc}}}{e \Delta B} \\ &\approx 2.8 \times 10^{24} \text{ cm}^2 \text{ s}^{-1} n_1^{-1/4} \gamma_7^{1/2} \left(\frac{L_f}{\text{pc}} \right)^{1/2}. \end{aligned} \quad (15)$$

For $\gamma > \gamma_{\text{esc}}$, namely for more energetic particles that we assume to be responsible for the X-ray emission, the diffusion occurs in the small-scale turbulence regime, in which $D(\gamma) = D(\gamma_{\text{esc}})(\gamma/\gamma_{\text{esc}})^2$ (Subedi et al. 2017). One can easily check that for the X-ray emitting particles the timescale for diffusive escape from the filament of length L_f is much longer than the timescale for synchrotron losses:

$$\begin{aligned} \tau_{\text{sync}}(\gamma_X) &= \frac{6\pi m c}{\sigma_T \Delta B^2 \gamma_X} \\ &\approx 115 \text{ yr} n_1^{-3/8} \gamma_7^{-3/4} E_{\text{X,keV}}^{-1/2} \left(\frac{L_f}{\text{pc}} \right)^{3/4}, \end{aligned} \quad (16)$$

where σ_T is the Thomson cross section and γ_X the Lorentz factor of the X-ray emitting particle. In the second equality, we used the relation between γ and peak synchrotron photon energy in the amplified field, and expressed the latter in keV as $E_{\text{X,keV}} = 1.5 \times 10^{-17} B_3 \gamma_X^2$.

3. Testing the scenario

We could now test the proposed scenario on some filaments for which all of the quantities listed above were measured with sufficient accuracy. We used the measured parameters of the system, listed in Table 1, to derive γ_{esc} from Eq. 10. We could then use γ_{esc} in Eq. 8 and estimate the value of ΔB . This also set the ratio, $\epsilon/\epsilon_{\text{lim}}$, through Eq. 6 and,

System	\dot{E} erg/s	τ_c kyr	d kpc	V_{psr} km/s	d_0 ''	$L_{X_1-X_2}$ erg/s (keV)	L_f pc (')	w_f pc (")	$\sin \theta_f$
Guitar ^{1, 2, 3}	1.27×10^{33}	1130	0.83	765.1	0.06	3.6×10^{30} (0.5-7)	0.6 (2.5)	0.08 (20)	115
Lighthouse ^{4, 5, 6}	1.36×10^{36}	116	7	800 – 2400	0.34	8.9×10^{33} (0.5-8) 1.9×10^{34} (3-79)	15 (7.5)	0.5 (16)	118
J2030+4415 ⁷	2.2×10^{34}	600	0.72*	290.6	0.3	7.5×10^{30} (0.5-7)	3.14 (15)	0.013 [†] (3.7)	130

Table 1. Relevant observational data of our benchmark systems. The main references are indicated next to the source name. \dot{E} is the pulsar’s spin-down power; τ_c its characteristic age; d its distance; and V_{psr} its projected velocity. d_0 is the bow shock standoff distance; $L_{X_1-X_2}$ indicates the X-ray luminosity of the feature in the energy range specified in parentheses; and L_f , w_f , and $\sin \theta_f$ are the feature’s length, width, and inclination, respectively. For the Lighthouse Nebula, we also report the X-ray luminosity in the 3-79 keV band recently measured by NuSTAR (Klingler et al. 2023).

* The distance is taken from the ATNF catalogue: www.atnf.csiro.au/people/pulsar/psrcat.

† The filament thickness appears to broaden with distance from the pulsar (de Vries & Romani 2022). Limiting the estimate to the first third of the filament, one finds that $w_f = 2''$, a thickness comparable with Chandra’s resolution.

¹de Vries et al. (2022), ²Deller et al. (2019), ³Chatterjee & Cordes (2002)

⁴Pavan et al. (2014), ⁵Pavan et al. (2016), ⁶Klingler et al. (2023)

⁷de Vries & Romani (2022).

once ϵ was estimated from X-ray measurements through Eq.14, we could finally constrain the size of the particle injection region, R , via Eq. 5. The results of this procedure are reported in Table 2.

The Guitar Nebula and its filament represent a prototypical case: this was the first system discovered (Hui & Becker 2007), and to date it is the best characterized, thanks to multi-epoch monitoring (de Vries et al. 2022). The Guitar Nebula is produced by the radio pulsar PSR B2224+65. Its bow shock is only visible in H_α emission (Chatterjee & Cordes 2002), and it has a peculiar guitar-like shape: in the $\sim 80''$ -long tail one can distinguish a thin, elongated head, followed by a wider body made by at least two bubbles. This peculiar shape has been interpreted as the result of mass loading of neutral atoms into the bow shock from a dense ambient medium (Morlino et al. 2015; Olmi et al. 2018). As was expected, given its age, the pulsar has a rather low \dot{E} , corresponding to a maximum Lorentz factor, $\gamma_{\text{MPD}} \simeq 1.2 \times 10^8$. The filament is ~ 0.6 pc long and shows a sharp leading edge (in the direction of motion of the pulsar) and a smoother trailing one, with hints of variation in the photon index (Johnson & Wang 2010) suggestive of synchrotron cooling (de Vries et al. 2022).

When we apply our model to the Guitar Nebula feature, we find that the amplified magnetic field, $\Delta B \approx 80 \mu\text{G}$, is produced by a current of particles, with $\gamma_{\text{esc}} \approx 0.1\gamma_{\text{MPD}}$, carrying a negligibly small fraction of the pulsar spin-down energy, $\epsilon \approx 6 \times 10^{-3}$. The amplified field also ensures that the Larmor radius of X-ray emitting particles, which we find to be a factor of ~ 3 more energetic than the current-carrying ones, is much smaller than the feature width, $R_L(\gamma_X)/w_f \approx 3 \times 10^{-3}$, which is consistent with our picture in which the latter is determined by synchrotron losses.

A final consistency check concerns the relative size of the injection region and the Larmor radius of escaping particles in the unperturbed magnetic field. If $R_L(\gamma_{\text{esc}}, B_0) \gg R$, the particles will occupy a much larger region of space than assumed in Eq. 2 and the current density will decrease proportionally. In fact, $R_L(\gamma_{\text{esc}}, B_0) = m c^2 \gamma_{\text{esc}} / (e B_0) \gg R$, but based on numerical simulations of the particle escape from these systems (Olmi & Bucciantini 2019), the flux of particles leaving the nebula is well collimated, and limited to a surface area of $\sim d_0^2$. Consistently, we find that the nec-

essary value of R is $R \approx d_0/2$ for the Guitar Nebula, implying a highly collimated initial particle flow, within an angle, $\alpha \sim R/R_L(\gamma_{\text{esc}}, B_0) \approx 3^\circ$. This initial anisotropy is quickly destroyed as the instability grows and full isotropization is also achieved for the more energetic X-ray emitting particles on a timescale, $t_{\text{iso}} \ll \tau_{\text{sync}}$ (see App. B), ensuring the validity of the assumptions underlying our calculations. In Fig. 1 we show how $\gamma_{\text{esc}}/\gamma_{\text{MPD}}$ and ϵ vary with n_{ISM} and V_{psr} , both depending on the uncertain estimate of the source distance.

In light of the encouraging results obtained for the Guitar, we applied our model to the other two systems with well-surveyed X-ray filaments, the Lighthouse Nebula (Pavan et al. 2016; Klingler et al. 2023) and PSR J2030+4415 (de Vries & Romani 2022). The filament associated with the powerful Lighthouse Nebula is the only one also observed in hard X-rays (Klingler et al. 2023), thanks to a recent NuSTAR campaign. The feature remains clearly visible up to ~ 25 keV, with a width and length compatible with those inferred from the higher-resolution Chandra data. The measurement of w_f along the feature is complicated by the observed striped morphology. Moreover, there is a large uncertainty on the pulsar speed, inferred from the association with a young (10–30 kyr) supernova remnant in the vicinity (Garcia et al. 2012). The Lighthouse feature is the longest one currently known and the only one showing a bent morphology. In our model, this bending is to be understood as a result of the GMF structure, being the length of the feature not much smaller than the presumed GMF correlation length of \sim tens pc. Focusing on the Chandra band, we find our model to be consistent with observations of the Lighthouse only if $V_{\text{psr}} \leq 1300 \text{ km s}^{-1}$, corresponding to $\Delta B \approx 26 \mu\text{G}$ and $\gamma_{\text{esc}} \approx 8 \times 10^7 (\approx \gamma_{X_1})$. A higher pulsar proper motion implies a higher magnetic field ($\Delta B \propto V_{\text{psr}}^{2/3}$ from Eq.8-10), and hence a lower γ_X ($\gamma_X \propto V_{\text{psr}}^{-1/3}$). At the same time, our method for estimating the density based on the standoff distance implies a number density of the ISM, $n_{\text{ISM}} \propto V_{\text{psr}}^{-2}$, and $\gamma_{\text{esc}} \propto V_{\text{psr}}^{7/3}$ (Eq. 10), so that, as V_{psr} increases, our assumption that $\gamma_X \geq \gamma_{\text{esc}}$ is soon violated. If, rather than estimating n_{ISM} as described above, we assume that (Pavan et al. 2014) $n_{\text{ISM}} = 0.1 \text{ cm}^{-3}$, then $\gamma_{\text{esc}} \propto V_{\text{psr}}^{4/3}$

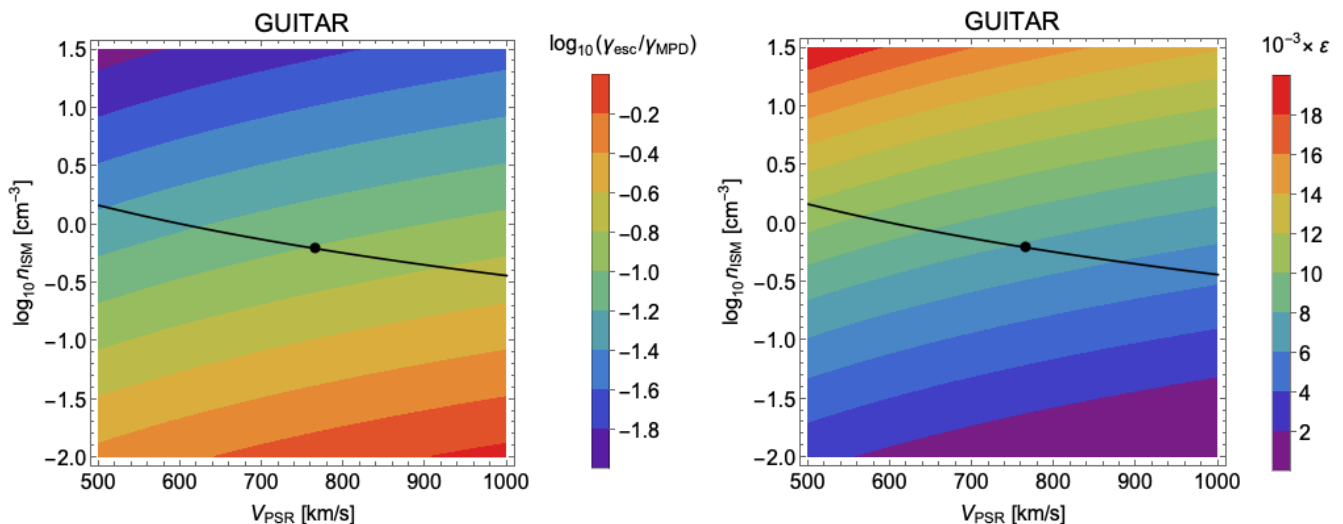


Fig. 1. Guitar Nebula: Color map of the ratio, $\gamma_{\text{esc}}/\gamma_{\text{MPD}}$ (base-10 logarithm, left panel), and the efficiency, ϵ (right panel), as a function of the pulsar velocity, V_{psr} (within the estimated uncertainty (de Vries et al. 2022)), and the ambient number density, n_{ISM} . The black curve shows the relation we used to estimate n_{ISM} (pressure equilibrium at the bow shock standoff distance, d_0). The black points indicate the position of the system for the best estimate of V_{psr} (and n_{ISM}).

and our model will work for¹ $V_{\text{psr}} \leq 1600 \text{ km s}^{-1}$. The range of validity of our model and the resulting value of $\gamma_{\text{esc}}/\gamma_{\text{MPD}}$ is shown in Fig. 2.

The very thin feature in J2030+4415 is powered by a γ -ray pulsar, with a spin-down luminosity corresponding to $\gamma_{\text{MPD}} = 5 \times 10^8$. Multi-epoch $\text{H}\alpha$ observations of the bow shock (de Vries & Romani 2022) clearly indicate an important rearrangement of the apex around $t_{\text{event}} \simeq 32 \text{ yr}$ ago, possibly due to a sudden variation in the ambient medium density, causing a compression of d_0 . If the observed w_f were determined by the synchrotron lifetime of the particles then, based on our model, we would estimate $\Delta B \approx 120 \mu\text{G}$ and $\gamma_{\text{esc}} \approx 10^8$, which would imply that $\tau_{\text{sync}} \sim 60 \text{ yr} > t_{\text{event}}$. However, it is difficult to believe that the feature was formed before t_{event} , so in this case we think that we are seeing all the particles that have been injected during t_{event} and $w_f = V_{\text{psr}} \sin \theta_f t_{\text{event}}$. In this scenario, we can only estimate boundaries for ΔB : the condition $t_{\text{event}} < t_{\text{sync}}$ implies that $\Delta B < 181 \mu\text{G}$, while the condition that X-ray emission must come from particles with $\gamma_X < \gamma_{\text{MPD}}$ implies that $\Delta B > 40 \mu\text{G}$. These boundaries, reported in Table 2, clearly show that the field must also be amplified by at least a factor of ~ 10 in this case. The right panel of Fig. 2 shows the relation between the amplified magnetic field, the pulsar speed, and the filament thickness of all three sources.

4. Discussion and conclusions

We claim that the filaments of non-thermal X-ray emission emerging from selected BSPWNe may be the first clear indication of the excitation of NRI due to a pencil beam current of charge-separated electrons (or positrons) leaving the parent nebulae. In two out of three cases, the length, thickness, and X-ray luminosity of the filaments can be well

¹ Notice however that values of $V_{\text{psr}} > 1600 \text{ km s}^{-1}$ are beyond 5σ of the peak velocity of the pulsar distribution (Faucher-Giguère & Kaspi 2006) and are only suggested based on the possible association of PSR J1101–6101 with SNR G290.0–0.8

accounted for. In the third case, due to the complex history of the source, it is only possible to derive boundaries on the magnetic field, which however imply efficient amplification, possibly explained by particles leaving the source at an energy close to the pulsar potential drop.

The amplified field should not however hinder the ballistic motion of the leptons, at least in the beginning, so as to allow the particles to populate the whole length of the filament. This is exactly what is expected to happen when the beam excites the NRI (Bell 2004). In order for the mechanism to work, particles' injection into the ISM needs to be collimated within a narrow range of pitch angles. The filaments are predicted to follow the structure of the large scale GMF at the location of the BSPWN.

The interpretation of the filaments in terms of excitation of the NRI by charge-separated electrons or positrons released by BSPWNe into the ISM is rich in implications. The amplified turbulence level can lead to extended confinement of the particles in selected regions around the sources, with implications for the pulsar's contribution to cosmic rays (CR) leptons (Schroer et al. 2023). In addition, it is tempting to speculate on a relation between the processes discussed here and the recently discovered phenomenon of TeV pulsar halos, regions of very high-energy ($\gtrsim \text{TeV}$) gamma-ray emission extending for tens of pc around a few pulsars (Abeysekara et al. 2017). In the halos, too, the particle transport seems to be suppressed by two to three orders of magnitude (López-Coto et al. 2022) compared with the Galactic values, as has been inferred from CR secondary and primary ratios (Schroer et al. 2023; Evoli et al. 2020), and the most obvious source of turbulence to explain the suppression seems to be the escaping particles themselves.

The recently discovered radio filaments around some bow shock nebulae (see e.g., Khabibullin et al. 2024) or the radio filaments observed in the Galactic center region (Yusef-Zadeh et al. 1984; Morris & Yusef-Zadeh 1985; Yusef-Zadeh & Morris 1987; Goedhart et al. 2023) may appear to be reminiscent of a similar process. However, the observed radio emission requires particles of much lower energy than the X-ray one ($\gamma \sim 10^4 - 10^5$), and no need to

System	n_{ISM} cm^{-3}	γ_{MPD}	γ_{esc}	ΔB μG	ϵ $\times 10^{-3}$	R/d_0
Guitar	0.6	1.2×10^8	1.2×10^7	78	6	0.5
Lighthouse	0.07	4.0×10^9	8×10^7	26	19	2
J2030+4415	4.0	5×10^8	$\lesssim 4 \times 10^7 (L_f/\text{pc})$	$40 < \Delta B < 181$	–	–

Table 2. Summary of the results for the three filaments considered. Here, n_{ISM} is the ambient number density, γ_{MPD} the Lorentz factor associated with the pulsar MPD, γ_{esc} the Lorentz factor of the particles producing the instability, ΔB the amplified magnetic field in the filament, ϵ the fraction of the pulsar power carried by the escaping particles, and R/d_0 the radius of the filament base, in terms of the bow shock standoff distance, d_0 . For J2030+4415 it is only possible to define a range for the amplified field, since there are indications that the filament formed only $t_{\text{event}} \sim 32$ yrs ago and its present w_f might not be determined by synchrotron losses. A lower limit comes from asserting that X-ray emission must be produced by particles with $\gamma \leq \gamma_{\text{MPD}}$, while an upper limit is derived from the condition $t_{\text{event}} < \tau_{\text{sync}}$ (see main text). From the maximum magnetic field, through Eq. 8 one also determines an upper limit of γ_{esc} , which depends on L_f , since the feature might not be in its final form.

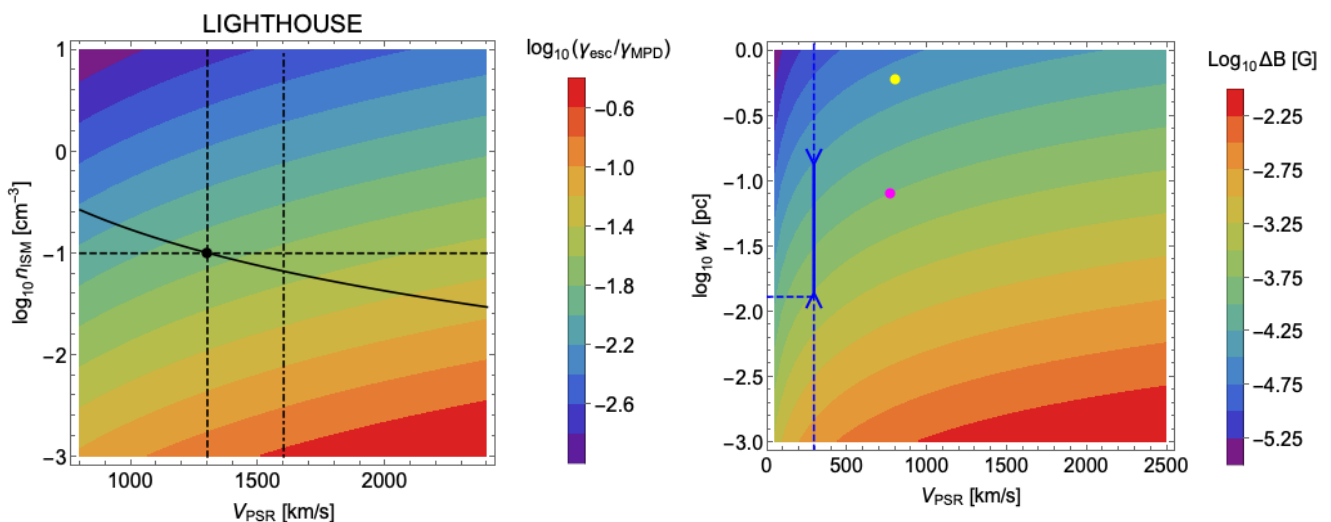


Fig. 2. *Left panel:* Color map of the ratio $\gamma_{\text{esc}}/\gamma_{\text{MPD}}$ (base-10 logarithm) for the Lighthouse Nebula, as a function of the pulsar velocity, V_{psr} , and ambient number density, n_{ISM} . The solid black curve shows the relation we used to estimate n_{ISM} (pressure equilibrium at the bow shock standoff distance, d_0). The black point indicates the position of the system based on the best estimate (Pavan et al. 2014) of n_{ISM} : $n_{\text{ISM}} = 0.1 \text{ cm}^{-3}$, $V_{\text{psr}} = 1300 \text{ km s}^{-1}$. The vertical lines mark the maximum value of V_{psr} that makes our model viable for $n_{\text{ISM}} = 0.1 \text{ cm}^{-3}$ ($V_{\text{psr,max}} = 1600 \text{ km s}^{-1}$, dash-dotted line).

Right panel: Color map of ΔB as a function of V_{psr} and w_f (uncertainties on the source distance reflect on both quantities). The best values for the Guitar and the Lighthouse Nebula are represented as magenta and yellow circles, respectively. The upper and lower limits obtained for J2030+4415 are shown as blue downward and upward arrows, respectively. The horizontal blue line shows the current filament thickness.

amplify the ambient magnetic field. Moreover, those particles can more efficiently escape the bow shock from the tail rather than the head (due to their smaller Larmor radii, Olmi & Bucciantini 2019), and then illuminate the pre-existing structures of the magnetic field (Barkov & Lyutikov 2019). Hence, we argue that these phenomena are most likely of a different origin than the filaments around BSPWNe.

Acknowledgements. This work has been partially funded by the European Union - Next Generation EU, through PRIN-MUR 2022TJW4EJ. B. Olmi, E. Amato and R. Bandiera also acknowledge support from the Italian National Institute for Astrophysics with PRIN-INAF 2019.

References

Abeysekara, A. U., Albert, A., Alfaro, R., et al. 2017, *Science*, 358, 911
Bandiera, R. 2008, *A&A*, 490, L3

Barkov, M. V. & Lyutikov, M. 2019, *MNRAS*, 489, L28
Bell, A. R. 2004, *MNRAS*, 353, 550
Bordas, P. & Zhang, X. 2020, *A&A*, 644, L4
Chatterjee, S. & Cordes, J. M. 2002, *ApJ*, 575, 407
de Vries, M. & Romani, R. W. 2020, *ApJ*, 896, L7
de Vries, M. & Romani, R. W. 2022, *ApJ*, 928, 39
de Vries, M., Romani, R. W., Kargaltsev, O., et al. 2022, *ApJ*, 939, 70
Deller, A. T., Goss, W. M., Brisken, W. F., et al. 2019, *ApJ*, 875, 100
Evoli, C., Morlino, G., Blasi, P., & Aloisio, R. 2020, *Phys. Rev. D*, 101, 023013
Faucher-Giguère, C.-A. & Kaspi, V. M. 2006, *ApJ*, 643, 332
García, F., Combi, J. A., Albacete-Colombo, J. F., et al. 2012, *A&A*, 546, A91
Goedhart, S., Cotton, W. D., Camilo, F., & the MeerKat coll. 2023, arXiv e-prints, arXiv:2312.07275
Hui, C. Y. & Becker, W. 2007, *A&A*, 467, 1209
Johnson, S. P. & Wang, Q. D. 2010, *MNRAS*, 408, 1216
Khabibullin, I. I., Churazov, E. M., Bykov, A. M., Chugai, N. N., & Zinchenko, I. I. 2024, *MNRAS*, 527, 5683
Klingler, N., Hare, J., Kargaltsev, O., Pavlov, G. G., & Tomsick, J. 2023, *ApJ*, 950, 177
Klingler, N., Kargaltsev, O., Pavlov, G. G., & Posselt, B. 2018, *ApJ*, 868, 119

- Klingler, N., Kargaltsev, O., Rangelov, B., et al. 2016, *ApJ*, 828, 70
- Klingler, N., Yang, H., Hare, J., et al. 2020, *ApJ*, 901, 157
- López-Coto, R., de Oña Wilhelmi, E., Aharonian, F., Amato, E., & Hinton, J. 2022, *Nature Astronomy*, 6, 199
- Marelli, M., Tiengo, A., De Luca, A., et al. 2019, *A&A*, 624, A53
- Medvedev, O. D., Karpova, A. V., Shibarov, Y. A., Zyuzin, D. A., & Pavlov, G. G. 2019, in *Journal of Physics Conference Series*, Vol. 1400, *Journal of Physics Conference Series*, 022018
- Morlino, G., Lyutikov, M., & Vorster, M. 2015, *MNRAS*, 454, 3886
- Morris, M. & Yusef-Zadeh, F. 1985, *AJ*, 90, 2511
- Olmi, B. 2023, *Universe*, 9, 402
- Olmi, B. & Bucciantini, N. 2019, *MNRAS*, 490, 3608
- Olmi, B. & Bucciantini, N. 2023, *PASA*, 40, e007
- Olmi, B., Bucciantini, N., & Morlino, G. 2018, *MNRAS*, 481, 3394
- Pavan, L., Bordas, P., Pühlhofer, G., et al. 2014, *A&A*, 562, A122
- Pavan, L., Pühlhofer, G., Bordas, P., et al. 2016, *A&A*, 591, A91
- Schroer, B., Evoli, C., & Blasi, P. 2023, *Phys. Rev. D*, 107, 123020
- Subedi, P., Sonsrtee, W., Blasi, P., et al. 2017, *ApJ*, 837, 140
- Temim, T., Slane, P., Kolb, C., et al. 2015, *ApJ*, 808, 100
- Torres, D. F., Cillis, A., Martín, J., & de Oña Wilhelmi, E. 2014, *Journal of High Energy Astrophysics*, 1, 31
- Yusef-Zadeh, F. & Morris, M. 1987, *ApJ*, 322, 721
- Yusef-Zadeh, F., Morris, M., & Chance, D. 1984, *Nature*, 310, 557
- Zhang, S., Zhu, Z., Li, H., et al. 2020, *ApJ*, 893, 3

Appendix A: Initial collimation of the particle beam

In the main text, we have shown that a good collimation – that is, small pitch angles – is one of the requirements for the formation of the observed filaments. A good collimation is also a natural outcome of the fact that the particles move from a region with a high magnetic field (the bow shock head),

$$\begin{aligned} B_{\text{head}} &\simeq \sqrt{24\pi(1-\eta)\rho_{\text{ISM}}} V_{\text{psr}} \simeq \\ &\simeq 400\sqrt{1-\eta}\sqrt{\frac{n_{\text{ISM}}}{0.5\text{ cm}^{-3}}}\left(\frac{V_{\text{psr}}}{500\text{ km s}^{-1}}\right)\mu\text{G}, \end{aligned} \quad (\text{A.1})$$

to a typical ISM magnetic field, around $3\mu\text{G}$ in magnitude. It is well known that, for particles with a small Larmor radius compared to the scale length of B variation, the enclosed magnetic flux is an adiabatic invariant and leads to the constancy of $B\sin^2\alpha$. Let us assume that, originally, the pitch angles of the escaping particles uniformly cover a 2π solid angle, equivalent to a mean value of $\sin\alpha = \pi/4$. This would imply, for the reference values given above, an average $\sin\alpha \simeq 0.07$. For the considered cases, the “small Larmor radius” approximation is valid, being the ratio of the gyro radius of the particles with energy γ_{esc} in the magnetic field of the bow shock head, $0.1 - 0.3 d_0 (B_{\text{head}}/100\mu\text{G})^{-1}$, where the bow shock standoff distance, d_0 , gives the scale of the variation in the field from the inside to the outside.

Appendix B: Delayed isotropization of X-ray emitting particles in the feature

Once the instability is saturated, the particles with energy, γ_{esc} , start to diffuse in the amplified magnetic field. One might wonder how much later this will also happen to the particles responsible for the emission at the X-rays, due to the fact that they have a larger Lorentz factor.

During its motion in the perturbed magnetic field, ΔB , a particle with Lorentz factor $\gamma_X > \gamma_{\text{esc}}$ will be deflected by an angle, $\Delta\theta_i = l/R_L^*(\gamma_X)$, on the interaction scale $l = 1/k_{\text{max}}^*$ and where $R_L^*(\gamma_X)$ is the Larmor radius of the particle in the amplified magnetic field. In a distance, L , the number of interactions (or deviations) that the particles experience is L/l . Then the total deflection can be estimated as $\Delta\theta = (L/l)^{1/2}l/R_L^*(\gamma_X)$. The isotropization length (L_{iso}), or the isotropization timescale ($t_{\text{iso}} \simeq L_{\text{iso}}/c$) is obtained by requiring that $\Delta\theta = 1$, so that

$$\begin{aligned} t_{\text{iso}} &\simeq \frac{L_{\text{iso}}}{c} = \frac{1}{\Omega_c} \frac{\gamma_X^2}{\gamma_{\text{esc}}} \left(\frac{\Delta B}{B_0}\right)^{-1} \simeq \\ &\simeq 0.01\text{ yr} \left(\frac{\gamma_{\text{esc}}}{10^7}\right)^{-1} \left(\frac{\Delta B}{50\mu\text{G}}\right)^{-2} \left(\frac{E_{\text{X,keV}}}{0.5\text{ keV}}\right). \end{aligned} \quad (\text{B.1})$$

With the typical lifetime of X-ray emitting particles in the amplified field being much longer than t_{iso} – namely, $\tau_{\text{synch}} \simeq 220\text{ yr} (\Delta B/50\mu\text{G})^{-3/2} (E_{\text{ph,keV}}/0.5\text{ keV})^{-1/2}$ – the distribution of particles can be safely assumed to be isotropic for the sake of computing the observed X-ray emission.